LUND UNIVERSITY

Source reconstruction by far-field data for imaging of defects in frequency selective radomes

Persson, Kristin; Gustafsson, Mats; Kristensson, Gerhard; Widenberg, Björn

2013

Total number of authors:
4

Source reconstruction by far-field data for imaging of defects in frequency selective radomes

Kristin Persson, Mats Gustafsson, Gerhard Kristensson, and Björn Widenberg

Kristin Persson, Mats Gustafsson, and Gerhard Kristensson
{Kristin.Persson,Mats.Gustafsson,Gerhard.Kristensson}@eit.lth.se

Department of Electrical and Information Technology
Electromagnetic Theory
Lund University
P.O. Box 118
SE-221 00 Lund
Sweden

Björn Widenberg
bjorn.widenberg@gknaerospace.com

Radomes & Antennas
GKN Aerospace Applied Composites
P.O Box 13070
SE-580 13 Linköping
Sweden

Abstract

In this paper, an inverse source reconstruction method with great potential in radome diagnostics is presented. Defects, *e.g.*, seams in large radomes, and lattice dislocations in frequency selective surface (FSS) radomes, are inevitable, and their electrical effects demand analysis. Here, defects in a frequency selective radome are analyzed with a method based on an integral formulation. Several far-field measurement series, illuminating different parts of the radome wall at 9.35 GHz, are employed to determine the equivalent surface currents and image the disturbances on the radome surface.

1   Introduction and background

Radomes enclose antennas to protect them from *e.g.*, weather conditions. Ideally, the radome is expected to be electrically transparent [10]. However, tradeoffs are necessary to fulfill properties such as aerodynamics, robustness, lightweight, weather persistency *etc.*. One tradeoff is the existence of defects. Specifically, seams appear when lightning strike protection and rain caps are applied, or in space frame radomes assembled by several panels [10, 18]. Other disturbances are Pitot tubes and the attachment of the radome to the hull of an aircraft. In all these examples of defects, it is essential to diagnose their influences, since they degrade the electromagnetic performance of the radomes if not carefully attended.

In this paper, we investigate if source reconstruction can be employed to localize and image defects on a radome surface. Employing far-field measurements remove the need for probe compensation [22]. An artificial puck plate (APP) radome with dislocations in the lattice is investigated. An APP radome is a frequency selective surface (FSS) designed to transmit specific frequencies [15, 21]. It consists of a thick perforated conducting frame, where the apertures in the periodic lattice are filled with dielectric pucks. These dielectric pucks act as short waveguide sections [15]. Due to the double curvature of an FSS surface, gaps and disturbances in the lattice may cause deterioration of the radome performance.

Source reconstruction methods determine the equivalent surface currents close to the object of interest. These methods have been utilized for various diagnostic purposes [1, 5, 8, 9, 11–14, 16, 17]. The reconstructions are established by employing a surface integral representation often in combination with a surface integral equation. The geometry of the object on which the fields are reconstructed is arbitrary. However, the problem is ill-posed and needs regularization.

Initial diagnostic studies are reported in [12–14], which focus on non-destructive radome diagnostics. The equivalent surface currents are reconstructed on a body of revolution with the method of moment (MoM), and the problem is regularized with a singular value decomposition (SVD). Other research groups have employed slightly different combinations of surface integral representations and surface integral equations to diagnose objects. Especially, radiation contributions from leaky cables are analyzed in [16], antennas are diagnosed in [1, 8, 9, 11, 17], and equivalent currents on a base station antenna are studied in [5]. A more detailed background of source reconstruction methods is found in [14].
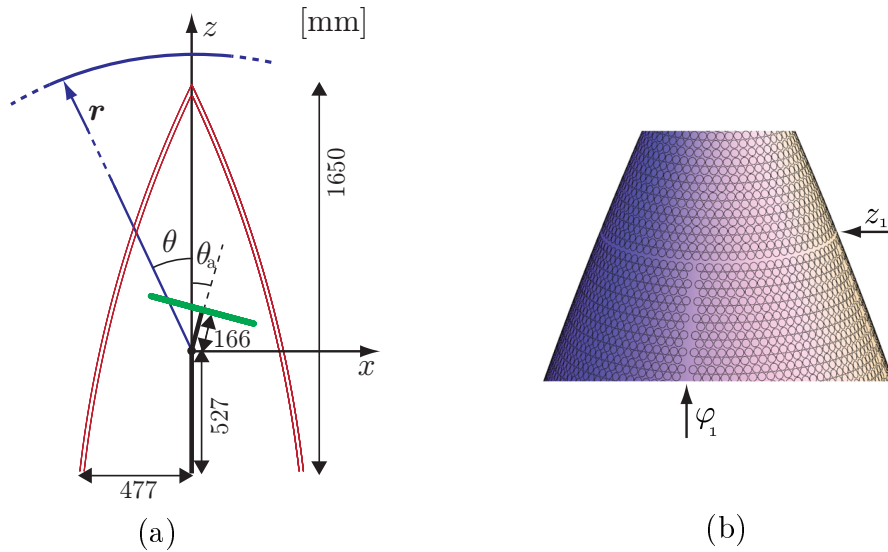
Figure 1: a) The geometry of the radome and the antenna. The center of rotation is located at the origin. b) Part of the radome visualizing the lattice structure and the defects at $\varphi_1 = -3°$ and $z_1 = 0.78\,\text{m}$.

This paper revisits the reconstruction algorithm described in [12, 14] in order to investigate if defects on an FSS radome can be imaged. In Sec. 2 we describe the far-field measurements, the set-up, and the measurement series. A brief reproduction of the algorithm is given in Sec. 3. Images and analysis of the reconstructed fields revealing the defects are found in Sec. 4, whereas a discussion of future possibilities and conclusions are presented in Sec. 5.

2   Measurement data and set-up

The aim of this paper is to back propagate a measured far field using an equivalent surface currents approach to determine the tangential field components on the radome surface. The purpose is to investigate if defects on a frequency selective surface (FSS) lattice can be localized.

The geometry of the radome and the antenna set-up are illustrated in Fig. 1a. The height of the radome corresponds to 51.4 wavelengths at the investigated frequency, 9.35 GHz. The antenna is a standard 18 inch slot antenna operating in the frequency band $9.2 - 9.5$ GHz. The radiated field is linearly polarized with a dominating electric field component in the horizontal y-direction, see Fig. 1a. Several mounting angles, defined by the polar angle θ_a, and the azimuth angle φ_a, are employed to illuminate different parts of the radome surface, see Fig. 1a.

The radome is an FSS structure with a disturbed periodic lattice, depicted in Fig. 1b. A vertical line defect — a column of elements is missing — is located at $\varphi_1 = -3°$. The defect ends at $z_1 = 0.78\,\text{m}$, where a horizontal line defect is located. The horizontal defect occurs due to a small vertical displacement of the elements. Owing to a large curvature of the radome, the horizontal defect also results in a
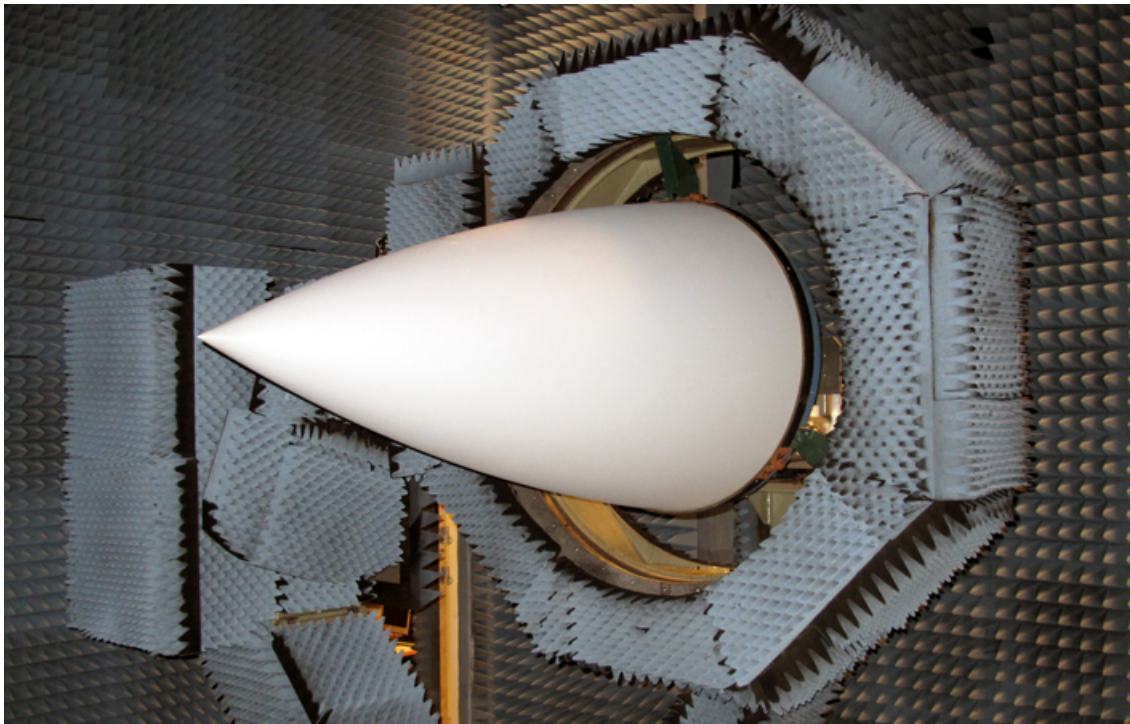
Figure 2: Photo of the radome in the compact test range.

small disturbance of the lattice in the azimuth direction. As a consequence, the vertical and horizontal defects are of different nature. Another horizontal defect is located at $z_0 = 0.38\,\mathrm{m}$, see Fig. 4a. The smaller curvature makes the disturbance of the lattice in the azimuth direction much smaller compared to the one at $z = z_1$.

Four different measurement series were performed, each with a different antenna orientation; $\{\theta_\mathrm{a} = 15°, \varphi_\mathrm{a} = 0°\}$, $\{\theta_\mathrm{a} = 12°, \varphi_\mathrm{a} = -20°\}$, $\{\theta_\mathrm{a} = 45°, \varphi_\mathrm{a} = 0°\}$, and $\{\theta_\mathrm{a} = 45°, \varphi_\mathrm{a} = -20°\}$. In the first two series, the antenna illuminates the area, where the vertical defect merges the horizontal defect at $z = z_1$, see Figs 1b and 4a. The illumination in the last two series highlights the lower cross, depicted in Fig. 4a. In this paper, we focus on the first two measurement series illuminating the top. The last two series are utilized as reference measurements to set the regularization parameter as described in [14]. Moreover, in the last series, a dielectric patch was attached to the radome surface, and the reconstruction of this patch was employed to verify the absolute position of the radome in the chamber. In each series illuminating the top, two different set-ups were measured for both polarizations. The antenna alone is referred to as configuration (0) whereas configuration (1) denotes the antenna together with the radome, also called the radome case. The configuration numbers are given as superscripts in the field notation in Sec. 4.

The far-field was measured at GKN Aerospace Applied Composites' compact test range in Linköping, Sweden, see Fig. 2 and [20]. The measurements were carried out over a spherical sector, described by the standard spherical coordinates, $\theta \in [0°, 120°]$ and $\varphi \in [0, 360°]$, see Fig. 1a for notation. The distance between two subsequent sample points was $1.5°$ in the azimuthal plane, and $0.75°$ in the polar plane, both
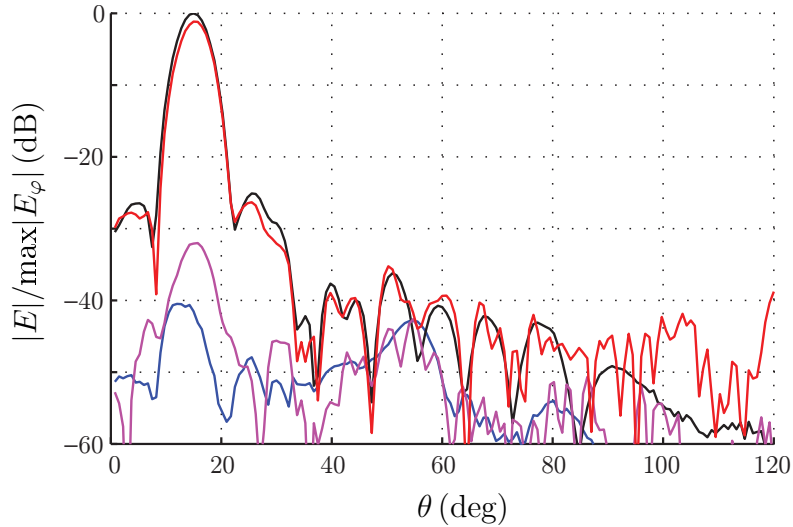
Figure 3: The measured far field through the main lobe when the antenna orientation is $\theta_{\mathrm{a}} = 15°$ and $\varphi_a = 0°$. The top two lines correspond to the co-component, $E = E_\varphi$, where the black line describes the antenna case and the red one the radome case. The lower two lines correspond to the cross-component, $E = E_\theta$, where the blue line describes the antenna case and the purple one the radome case.

fulfilling the sample criteria [6, 22]. More details concerning the measurements and the chamber are found in [14, 20].

Both polarizations of the measured far field, with and without the radome, are given in Fig. 3, where the antenna orientation is $\theta_{\mathrm{a}} = 15°$ and $\varphi_a = 0°$. The cross section in the polar plane, through the main lobe, $\varphi = 0$, is shown. The radome changes the main lobe of the co-polarization, E_φ, indicating transmission loss and beam deflection. The near side lobe levels are also slightly changed. Scattering effects, at large polar angles, are introduced by the radome and affect the far outside lobes in the co-polarization. The radome also changes the lobes of the cross-polarization. Bear in mind, that the antenna illuminates the top of the radome, *i.e.*, it is likely that multiple scattering inside the radome give rise to some of the changes. Moreover, it is not possible to determine the electrical influence of the defects from the unprocessed far-field data, *i.e.*, a reconstruction technique, to retrieve the fields on the radome surface, is necessary. The far fields, when the antenna orientation is $\theta_{\mathrm{a}} = 12°$ and $\varphi_a = 20°$, show similar deviations as the ones in Fig. 3.

3 Reconstruction algorithm

To investigate if a source reconstruction technique can be applied to image defects on a frequency selective surface (FSS) radome, a reconstruction algorithm is applied to relate the tangential electromagnetic fields on the radome surface to the measured far field described in Sec. 2. In this paper, we only give a short outline of the algorithm and some key implementation aspects, since the algorithm is thoroughly

described in previous works, see [12, 14].

The electric surface integral equation (EFIE) [7]

$$\hat{\boldsymbol{n}}(\boldsymbol{r}) \times \left\{ \mathcal{L}\left(\eta_0 \boldsymbol{J}\right)(\boldsymbol{r}) - \mathcal{K}\left(\boldsymbol{M}\right)(\boldsymbol{r}) \right\} = \frac{1}{2}\boldsymbol{M}(\boldsymbol{r}) \tag{3.1}$$

where $\boldsymbol{r} \in S_{\text{radome}}$, and S_{radome} denotes the radome surface, smoothly closed at the bottom, is combined with the surface integral representation [4, 19]

$$\begin{bmatrix}\hat{\boldsymbol{\theta}}(\boldsymbol{r})\\\hat{\boldsymbol{\varphi}}(\boldsymbol{r})\end{bmatrix} \cdot \left\{ -\mathcal{L}\left(\eta_0 \boldsymbol{J}\right)(\boldsymbol{r}) + \mathcal{K}\left(\boldsymbol{M}\right)(\boldsymbol{r}) \right\} = \begin{bmatrix}\hat{\boldsymbol{\theta}}(\boldsymbol{r}) \cdot \boldsymbol{E}(\boldsymbol{r})\\\hat{\boldsymbol{\varphi}}(\boldsymbol{r}) \cdot \boldsymbol{E}(\boldsymbol{r})\end{bmatrix} \tag{3.2}$$

where $\boldsymbol{r}$ belongs to the set of measurement points, see Fig. 1a, and η_0 is the intrinsic wave impedance of free space. A combination of the integral representation (3.2) with a magnetic field integral equation (MFIE) does not change the results in Sec. 4 significantly. The far field is measured over a spherical sector, described by the two spherical orthogonal components, $\hat{\boldsymbol{\varphi}}$ (azimuth) and $\hat{\boldsymbol{\theta}}$ (polar), $cf.$, Sec. 2. The operators introduced in (3.1)–(3.2) are [7]

$$\mathcal{L}(\boldsymbol{X})(\boldsymbol{r}) = \mathrm{j}k \iint\limits_{S_{\text{radome}}} \left\{ g(\boldsymbol{r}',\boldsymbol{r})\boldsymbol{X}(\boldsymbol{r}') - \frac{1}{k^2}\,\nabla' g(\boldsymbol{r}',\boldsymbol{r})\big[\nabla'_S \cdot \boldsymbol{X}(\boldsymbol{r}')\big] \right\} \mathrm{d}S'$$

and

$$\mathcal{K}(\boldsymbol{X})(\boldsymbol{r}) = \iint\limits_{S_{\text{radome}}} \nabla' g(\boldsymbol{r}',\boldsymbol{r}) \times \boldsymbol{X}(\boldsymbol{r})\,\mathrm{d}S'$$

where g is the scalar free space Green's function, k is the wave number, and $\nabla_S \cdot$ denotes the surface divergence [4]. Also, the equivalent surface currents on the radome surface are, $\boldsymbol{J} = \hat{\boldsymbol{n}} \times \boldsymbol{H}$ and $\boldsymbol{M} = -\hat{\boldsymbol{n}} \times \boldsymbol{E}$ [7]. The equivalent surface currents on the radome surface are decomposed into two tangential components along the horizontal, $\hat{\boldsymbol{\varphi}}$, and vertical, $\hat{\boldsymbol{v}}$, arc lengths coordinates, $i.e.$, $[\hat{\boldsymbol{\varphi}}, \hat{\boldsymbol{v}}, \hat{\boldsymbol{n}}]$ form a right-handed coordinate system. Throughout the paper we use the notations, $H_{\text{v}} = \boldsymbol{H} \cdot \hat{\boldsymbol{v}} = -J_{\varphi}$, $H_{\varphi} = \boldsymbol{H} \cdot \hat{\boldsymbol{\varphi}} = J_{\text{v}}$, $E_{\varphi} = \boldsymbol{E} \cdot \hat{\boldsymbol{\varphi}} = -M_{\text{v}}$, and $E_{\text{v}} = \boldsymbol{E} \cdot \hat{\boldsymbol{v}} = M_{\varphi}$ for the reconstructed tangential fields.

The set-up is axially symmetric, $i.e.$, a body of revolution MoM code and a Fourier expansion of the fields can be employed. Only components with Fourier index $m \in [-71, 71]$ are relevant to solve (3.1)–(3.2). The problem is regularized by a singular value decomposition (SVD), where the regularization parameter is set by the reference measurement series. The far-field radius, r in Fig. 1a, is set to 2200 m. Employing larger radii do not change the results significantly. More details, parameter choices of the MoM code, and discussions about the regularization parameter are found in [14].

4   Reconstruction results

Two measurement series are investigated at 9.35 GHz with the antenna orientations: $\{\theta_{\text{a}} = 15°, \varphi_{\text{a}} = 0°\}$, and $\{\theta_{\text{a}} = 12°, \varphi_{\text{a}} = -20°\}$, respectively, $cf.$, Fig. 1a. The

vertical lattice disturbance at $\varphi = \varphi_1$, and the horizontal one at $z = z_1$ are illuminated, $cf.$, Fig. 1b and Sec. 2. The magnetic field components, co-polarization H_v and cross-polarization H_φ, are depicted since they give clearer images of the defects, see also [14].

The calculated tangential fields are visualized in Fig. 4, where the antenna orientation is $\theta_a = 15°$ and $\varphi_a = 0°$. In Figs 4ac, the field from the antenna is depicted on a surface shaped as the radome to show how the defects, marked as white lines, are illuminated. The z-axis in Fig. 4a, gives the positions of the horizontal defects, $i.e.$, $z_0 = 0.38\,\mathrm{m}$ and $z_1 = 0.78\,\mathrm{m}$, and the zooming area adapted throughout the paper, $i.e.$, $z_z \geq 0.28\,\mathrm{m}$. The vertical defect and its top ending at z_1 appear in the field of the co-polarization on the radome, see Fig. 4b. The cross-polarized field reveals the horizontal defect at z_1, see Fig. 4d. The amplitude difference between the co- and cross-polarization, $i.e.$, $20\log|H_v^{(0)}|_{\max} - 20\log|H_\varphi^{(0)}|_{\max}$, is $4.2\,\mathrm{dB}$, where log denotes the 10-base logarithm and $|H_{v/\varphi}^{(0)}|_{\max} = \max\limits_{\boldsymbol{r} \in S_{\mathrm{radome}}} |H_{v/\varphi}^{(0)}(\boldsymbol{r})|$.

To verify that the defects really are imaged in Figs 4bd, another measurement series was performed, where the antenna orientation is $\theta_a = 12°$ and $\varphi_a = -20°$. The influence of the radome in the main lobe is visualized in Figs 5–10. In Fig. 5, the field amplitudes are depicted. Even though the main lobe is rotated by $\Delta\theta = -3°$ and $\Delta\varphi = -20°$, the positions of the vertical defects (Figs 5ac), as well as the horizontal ones (Figs 5bd), are identical. The linear scale reveals that the defects block the field. The images of the cross-polarization, Figs 5bd, indicate an interference pattern caused by the defects, where the distance between two subsequent minima is approximately one wavelength.

The phase difference between the antenna and radome cases, the insertion phase delay (IPD), is an essential tool in diagnosing dielectric radomes [3, 14]. Here, we investigate if defects in a frequency selective surface (FSS) lattice can be discovered or not. Fig. 6 visualizes the IPD for the two antenna orientations. Observe that the IPD is only determined modulus 2π, the phase difference $\angle H^{(0)} - \angle H^{(1)} = \frac{180}{\pi}\angle\{H_v^{(0)}[H_v^{(1)}]^*\}$ gives a positive phase shift due to the time convention $\mathrm{e}^{\mathrm{j}\omega t}$ used, and the star denotes the complex conjugate. The images of the vertical defect, corresponding to the two different antenna orientations, are consistent in Figs 6ac. Moreover, the position of the horizontal defect is stable in Figs 6bd. The phase reconstruction is not reliable in areas with low amplitudes. To suppress the noise in these areas, a mask is imposed in the figures, which only shows areas where the field from the antenna, $H_{v/\varphi}^{(0)}$, is greater than a predefined value. Specifically, $20\log\{|H_v^{(0)}|/|H_v^{(0)}|_{\max}\} \geq -15\,\mathrm{dB}$ in Figs 6ac and $20\log\{|H_\varphi^{(0)}|/|H_\varphi^{(0)}|_{\max}\} \geq -10\,\mathrm{dB}$ in Figs 6bd, respectively, where $H_{v/\varphi}^{(0)}$ are depicted in Figs 4ac.

A diffraction pattern is detected in both polarizations, which implies an IPD fluctuation in the main lobe. Due to rather large angles of incidence, $cf.$, Fig. 1a, the IPDs of the co- and cross-components deviate from each other [3]. In the main lobe, the cross-polarization, H_φ, has an average phase shift of $130°$ and the co-polarization, H_v, has an average phase shift of $160°$. The vertical defect alters the IPD with an additional $20° - 30°$. As a consequence of the large phase shifts in the radome wall, the absolute difference $|H_{v/\varphi}^{(1)} - H_{v/\varphi}^{(0)}|$ becomes impertinent as a

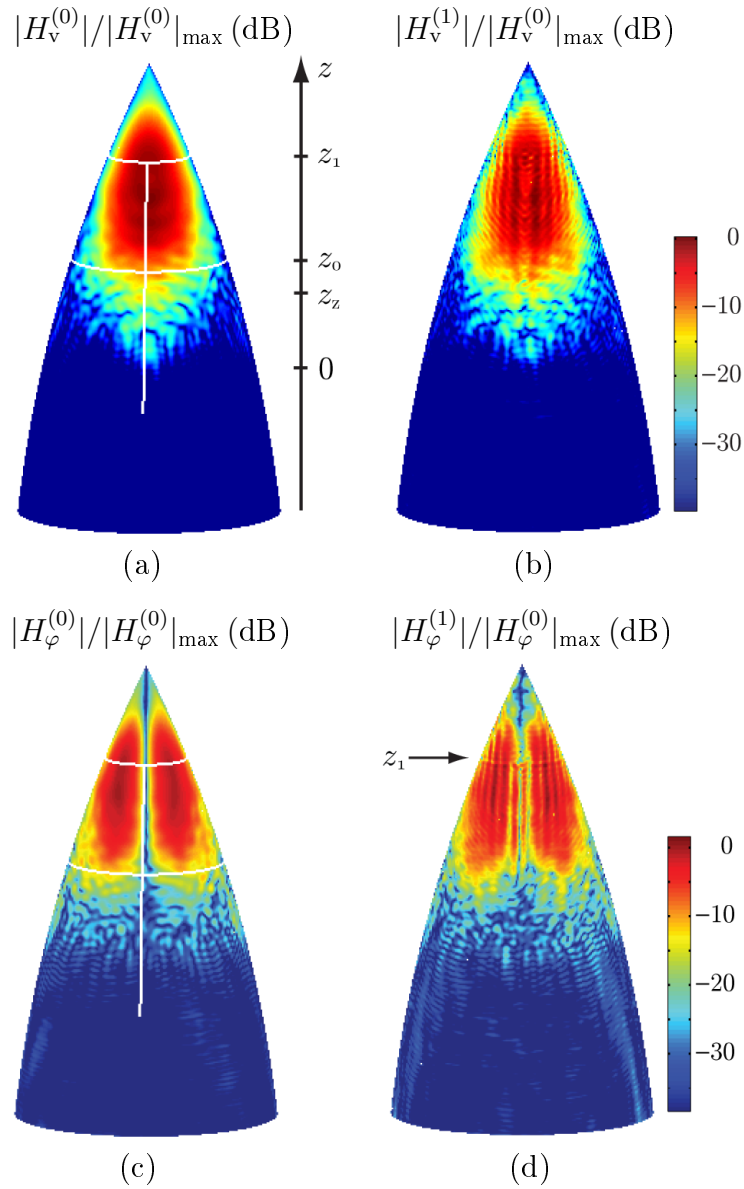**Figure 4**: The H_{v}- and H_{φ}-components of the antenna alone, *i.e.*, conf. (0), are depicted in (a) and (c), respectively. The defects at z_0 and z_1, marked with white lines, are shown. Figs (b) and (d) show the H_{v}- and H_{φ}-components of the radome case, *i.e.*, conf. (1). The antenna orientation is $\theta_{\mathrm{a}} = 15°$ and $\varphi_a = 0°$.

$$(|H_{\mathrm{v}}^{(1)}|-|H_{\mathrm{v}}^{(0)}|)/|H_{\mathrm{v}}^{(0)}|_{\max} \qquad (|H_{\varphi}^{(1)}|-|H_{\varphi}^{(0)}|)/|H_{\varphi}^{(0)}|_{\max}$$

(a) (b)

$$(|H_{\mathrm{v}}^{(1)}|-|H_{\mathrm{v}}^{(0)}|)/|H_{\mathrm{v}}^{(0)}|_{\max} \qquad (|H_{\varphi}^{(1)}|-|H_{\varphi}^{(0)}|)/|H_{\varphi}^{(0)}|_{\max}$$
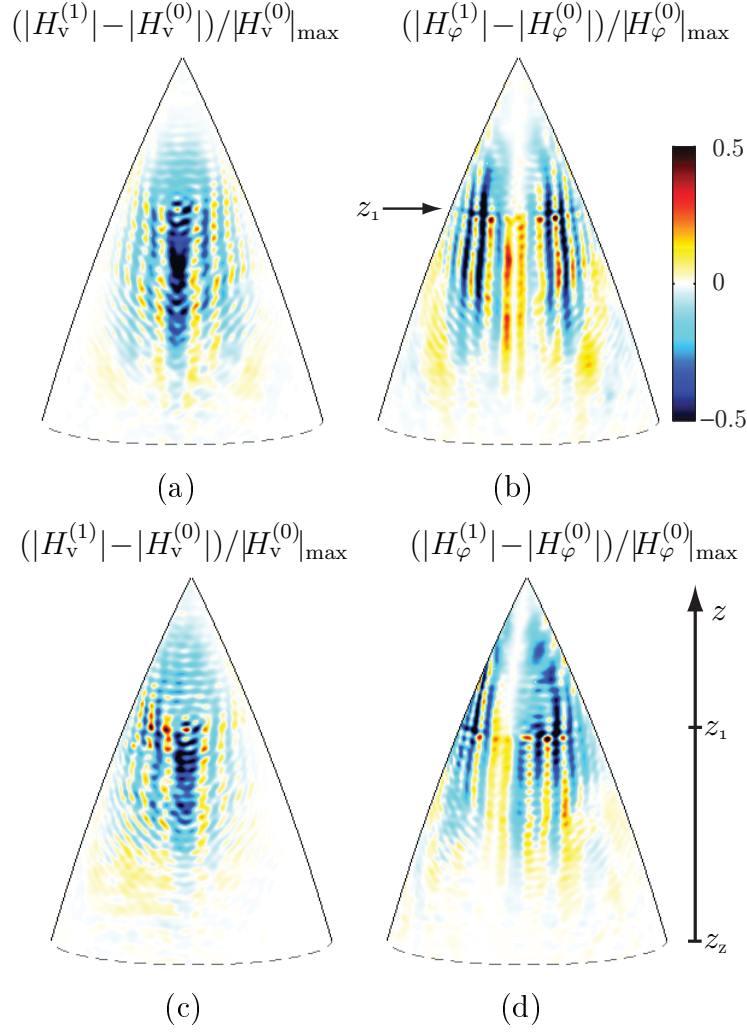
(c) (d)

Figure 5: The reconstructed amplitude differences between the radome case and the antenna alone for $z \geq z_{\mathrm{z}}$. The top row (ab) corresponds to the antenna orientation $\theta_{\mathrm{a}} = 15°$ and $\varphi_a = 0°$, whereas the bottom row (cd) corresponds to $\theta_{\mathrm{a}} = 12°$ and $\varphi_a = -20°$. Figs (ac) show the H_{v}-component and (bd) the H_{φ}-component, respectively.

visualization tool to detect differences. The reason for this is that a phase shift close to π adds the fields instead of subtracting them.

As previously stated, the defects seem to block the incoming field, *cf.*, Fig. 5. This obstruction, which was detected in the magnetic field, is also visible in the power flow. The real part of Poynting's vector describes the time average power density that flows through the radome surface. In the right-handed coordinate system on the radome surface, $[\hat{\boldsymbol{\varphi}}, \hat{\boldsymbol{v}}, \hat{\boldsymbol{n}}]$, the normal component of Poynting's vector is [2]

$$P = \frac{1}{2}\,\mathrm{Re}\left\{\boldsymbol{E} \times \boldsymbol{H}^*\right\} \cdot \hat{\boldsymbol{n}} = \frac{1}{2}\,\mathrm{Re}\left\{E_{\varphi}H_{\mathrm{v}}^* - E_{\mathrm{v}}H_{\varphi}^*\right\} \equiv P_{\mathrm{n}}^{\mathrm{co}} + P_{\mathrm{n}}^{\mathrm{cross}} \qquad (4.1)$$

where the star denotes the complex conjugate. In Fig. 7a, the difference in the power flow between the radome and the antenna alone is depicted. This image illustrates the impact of the radome. Moreover, it filters out some of the interference pattern,
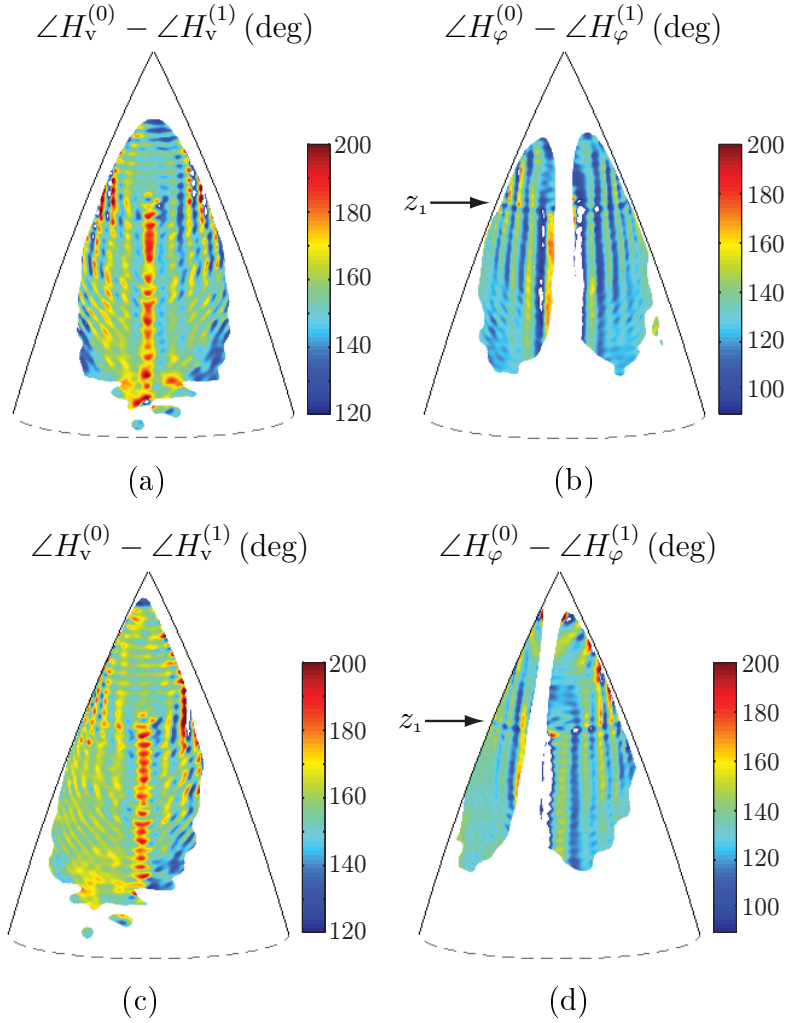
$$\angle H_{\mathrm{v}}^{(0)} - \angle H_{\mathrm{v}}^{(1)} \text{ (deg)} \qquad \angle H_{\varphi}^{(0)} - \angle H_{\varphi}^{(1)} \text{ (deg)}$$

(a)   (b)

$$\angle H_{\mathrm{v}}^{(0)} - \angle H_{\mathrm{v}}^{(1)} \text{ (deg)} \qquad \angle H_{\varphi}^{(0)} - \angle H_{\varphi}^{(1)} \text{ (deg)}$$

(c)   (d)

Figure 6: The insertion phase delay, IPD, $\angle H_{\mathrm{v}/\varphi}^{(0)} - \angle H_{\mathrm{v}/\varphi}^{(1)}$ for $z \geq z_{\mathrm{z}}$. The top row (ab) corresponds to the antenna orientation $\theta_{\mathrm{a}} = 15°$ and $\varphi_a = 0°$, whereas the bottom row (cd) corresponds to $\theta_{\mathrm{a}} = 12°$ and $\varphi_a = -20°$. Figs (ac) show the H_{v}-component in areas illuminated down to $-15\,\mathrm{dB}$, whereas (bd) visualize the H_{φ}-component in areas illuminated down to $-10\,\mathrm{dB}$.

and gives a clear view of the vertical defect. To reduce the influence of a non-even illumination, a pointwise normalization of the power flow, *i.e.*, a normalization with $P^{(0)}(\boldsymbol{r})$, is presented in Fig. 7b. A mask of $10\log\{P^{(0)}/P_{\max}^{(0)}\} \geq -15\,\mathrm{dB}$ is imposed, to avoid amplification of small fields in areas of low illumination. In this normalization, the horizontal defect starts to emerge. The reason why the horizontal defect is less visible in the power flow graphs is that this defect is perceived by the weaker cross-components, H_{φ} and E_{v}, and these components are suppressed by the stronger co-components in (4.1). To investigate if it is possible to get a more distinct view of the horizontal defect, the part of P with contributions from only the cross-components, *i.e.*, P^{cross} in (4.1), is mapped. This quantity is visualized in Fig. 8a, where the horizontal defect appears. An even more distinct image is obtained if the field difference, pointwise normalized with the incidence field, is depicted, see
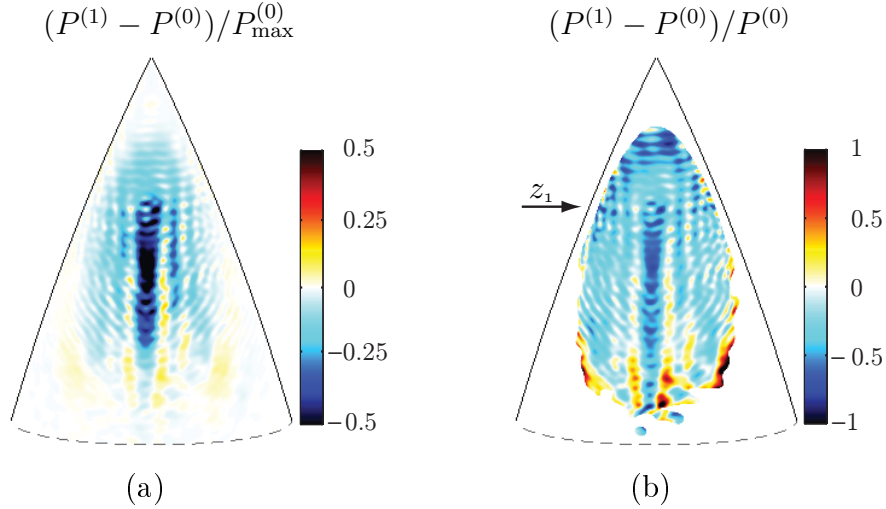
$$(P^{(1)} - P^{(0)})/P_{\max}^{(0)} \qquad\qquad (P^{(1)} - P^{(0)})/P^{(0)}$$

(a)   (b)

Figure 7: The time average power density through the radome for $z \geq z_z$. The antenna orientation is $\theta_a = 15°$ and $\varphi_a = 0°$. a) Normalized to the maximum value. b) Pointwise normalization in the illuminated areas down to $-15\,\mathrm{dB}$.

Fig. 8b. All values $15\,\mathrm{dB}$ below the maximum of $P^{(0)\mathrm{cross}}$ are suppressed. Similar results are obtained when the antenna orientation is $\theta_a = 12°$ and $\varphi_a = -20°$, see Figs 9–10. The positions of the defects are consistent in Figs 7–10, whereas the rest of the field pattern changes slightly when the illumination is moved.

So far, the two measurement series illuminating the top have been investigated. The measurements focusing on the lower cross at $z = z_0$ are not presented in detail here, see Fig. 4a and a description in Sec. 2. However, some of the results are worth mentioning. For example, the horizontal defect at $z = z_0$ is hardly visible. The lattice is not as disturbed in the azimuth direction as it is higher up on the radome surface, and it is conjectured that this explains the weak effects, *cf.*, discussion in Sec. 2. Moreover, the diffraction pattern — clearly visible in Figs 5bd, where the top is investigated — does not appear in the cross-polarization for the lower illumination. Additionally, a flash lobe is present, revealing a vertical defect on the back of the radome wall.

5   Conclusions and discussions

Defects, giving rise to pattern distortions, are often an inevitable tradeoff in the design of radomes. To minimize the effects of these defects, diagnostic tools are valuable in the evaluation process and performance verification. In this paper, an inverse source reconstruction method is utilized to back propagate measured far-field to the surface of a frequency selective surface (FSS) radome with defects in its lattice, see Fig. 1b. Different illuminations of the radome wall help us to image these defects.

Both the amplitude and the phase differences are investigated. A vertical line defect, where a column of elements is missing, is clearly visible in the images of the magnetic co-polarization. Moreover, the visualizations of the magnetic cross-polarization reveal a horizontal line defect caused by an enlarged vertical distance
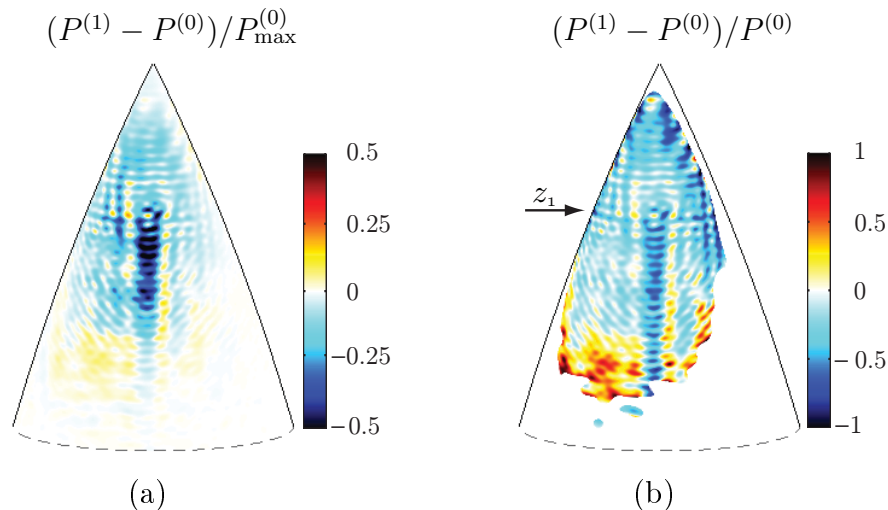
$$(P^{(1)\mathrm{cross}} - P^{(0)\mathrm{cross}})/P_{\max}^{(0)\mathrm{cross}}$$

$$(P^{(1)\mathrm{cross}} - P^{(0)\mathrm{cross}})/P^{(0)\mathrm{cross}}$$

(a)   (b)

Figure 8: The cross-components of Poynting's vector for $z \geq z_z$. The antenna orientation is $\theta_a = 15°$ and $\varphi_a = 0°$. a) Normalized to the maximum value. b) Pointwise normalization and viewed in areas illuminated down to $-15\,\mathrm{dB}$.

between the center of the lattice elements. It is conjectured that the defects are blocking the field, and images of the power flow, *i.e.*, the real part of Poynting's vector, confirm this hypothesis.

Prior studies have shown the potential of the source reconstruction method as a useful tool in non-destructive dielectric radome diagnostics [12–14]. It is concluded that also defects on FSS radomes can be properly analyzed with the same technique. Further studies will address the question regarding the origin of the diffraction pattern together with a thorough analysis of the measurement data illuminating the lower cross. Another interesting aspect to be investigated is why the defects are visible in specific field components and not in others. Also, the diagnostics of other defects caused by *e.g.*, lightning strike protection or edges, are to be reported elsewhere.

6 Acknowledgement

References

[1] Y. Alvarez, F. Las-Heras, and C. Garciain. The sources reconstruction method for antenna diagnostics and imaging applications. In A. Kishk, editor, *Solutions and Applications of Scattering, Propagation, Radiation and Emission of Electromagnetic Waves*. InTech, 2012.

Figure 9: The time average power density through the radome for $z \geq z_{\mathrm{z}}$. The antenna orientation is $\theta_{\mathrm{a}} = 12°$ and $\varphi_a = -20°$. a) Normalized to the maximum value. b) Pointwise normalization and viewed in areas illuminated down to $-15\,\mathrm{dB}$.

[2] C. A. Balanis. *Antenna Theory*. John Wiley & Sons, New Jersey, third edition, 2005.

[3] D. G. Burks. Radomes. In J. L. Volakis, editor, *Antenna engineering handbook*. pub-mcgraw, fourth edition, 2007.

[4] D. Colton and R. Kress. *Integral Equation Methods in Scattering Theory*. John Wiley & Sons, New York, 1983.

[5] T. F. Eibert, E. Kaliyaperumal, C. H. Schmidt, et al. Inverse equivalent surface current method with hierarchical higher order basis functions, full probe correction and multilevel fast multipole acceleration. *Progress In Electromagnetics Research*, **106**, 377–394, 2010.

[6] J. E. Hansen, editor. *Spherical Near-Field Antenna Measurements*. Number 26 in IEE electromagnetic waves series. Peter Peregrinus Ltd., Stevenage, UK, 1988. ISBN: 0-86341-110-X.

[7] J. M. Jin. *Theory and computation of electromagnetic fields*. Wiley Online Library, 2010.

[8] E. Jörgensen, D. W. Hess, P. Meincke, O. Borries, C. Cappellin, and J. Fordham. Antenna diagnostics on planar arrays using a 3D source reconstruction technique and spherical near-field measurements. In *Antennas and Propagation (EUCAP), 2012 6th European Conference on*, pages 2547–2550. IEEE, 2012.

[9] E. Jörgensen, P. Meincke, and C. Cappellin. Advanced processing of measured fields using field reconstruction techniques. In *Antennas and Propagation (EUCAP), Proceedings of the 5th European Conference on*, pages 3880–3884. IEEE, 2011.
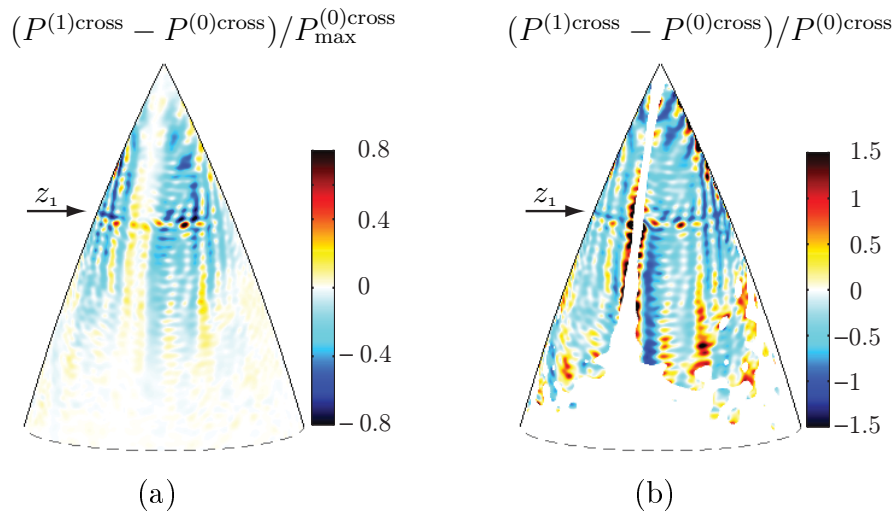
$$(P^{(1)\mathrm{cross}} - P^{(0)\mathrm{cross}})/P_{\max}^{(0)\mathrm{cross}} \qquad (P^{(1)\mathrm{cross}} - P^{(0)\mathrm{cross}})/P^{(0)\mathrm{cross}}$$

(a)   (b)

Figure 10: The cross-components of Poynting's vector for $z \geq z_z$. The antenna orientation is $\theta_a = 12°$ and $\varphi_a = -20°$. a) Normalized to the maximum value. b) Pointwise normalization and viewed in areas illuminated down to $-15\,\mathrm{dB}$.

[10] D. J. Kozakoff. *Analysis of Radome-Enclosed Antennas*. Artech House, Boston, London, 1997.

[11] Y. A. Lopez, F. Las-Heras Andres, M. R. Pino, and T. K. Sarkar. An improved super-resolution source reconstruction method. *Instrumentation and Measurement, IEEE Transactions on*, **58**(11), 3855–3866, 2009.

[12] K. Persson, M. Gustafsson, and G. Kristensson. Reconstruction and visualization of equivalent currents on a radome using an integral representation formulation. *Progress In Electromagnetics Research*, **20**, 65–90, 2010.

[13] K. Persson and M. Gustafsson. Reconstruction of equivalent currents using a near-field data transformation – with radome applications. *Progress in Electromagnetics Research*, **54**, 179–198, 2005.

[14] K. Persson, M. Gustafsson, G. Kristensson, and B. Widenberg. Radome diagnostics — source reconstruction of phase objects with an equivalent currents approach. Technical Report LUTEDX/(TEAT-7223)/1–22/(2012), Lund University, Department of Electrical and Information Technology, P.O. Box 118, S-221 00 Lund, Sweden, 2012. http://www.eit.lth.se.

[15] S. Poulsen. *Stealth radomes*. PhD thesis, Lund University, Department of Electroscience, Lund University, P.O. Box 118, S-221 00 Lund, Sweden, 2006.

[16] J. L. A. Quijano, L. Scialacqua, J. Zackrisson, L. J. Foged, M. Sabbadini, and G. Vecchi. Suppression of undesired radiated fields based on equivalent currents reconstruction from measured data. *Antennas and Wireless Propagation Letters, IEEE*, **10**, 314–317, 2011.

[17] J. L. A. Quijano and G. Vecchi. Field and source equivalence in source reconstruction on 3D surfaces. *Progress In Electromagnetics Research*, **103**, 67–100, 2010.

[18] R. Shavit, A. P. Smolski, E. Michielssen, and R. Mittra. Scattering analysis of high performance large sandwich radomes. *IEEE Transactions on Antennas and Propagation*, **40**(2), 126–133, 1992.

[19] S. Ström. Introduction to integral representations and integral equations for time-harmonic acoustic, electromagnetic and elastodynamic wave fields. In V. V. Varadan, A. Lakhtakia, and V. K. Varadan, editors, *Field Representations and Introduction to Scattering*, volume 1 of *Handbook on Acoustic, Electromagnetic and Elastic Wave Scattering*, chapter 2, pages 37–141. Elsevier Science Publishers, Amsterdam, 1991.

[20] B. Widenberg. Advanced compact test range for both radome and antenna measurement. In *11th European Electromagnetic Structures Conference*, pages 183–186, Torino, Italy, 2005.

[21] T. K. Wu, editor. *Frequency Selective Surface and Grid Array*. John Wiley & Sons, New York, 1995.

[22] A. D. Yaghjian. An overview of near-field antenna measurements. *IEEE Trans. Antennas Propagat.*, **34**(1), 30–45, January 1986.